Article

Influence of Aliovalent Cation Substitution and Mechanical Compression on Li-Ion Conductivity and Diffusivity in Argyrodite Solid Electrolytes

Parvin Adeli, J. David Bazak, Ashfia Huq, Gillian R. Goward,* and Linda F. Nazar*

Read Online

ACCESS | Metrics & More | Article Recommendations | SI Supporting Information

ABSTRACT: All-solid-state batteries employing sulfide superionic conductors demand new electrolyte materials with excellent Li-ion transport properties. We report on dual-modified superionic conductors in the Li-argyrodite family. In these materials prepared by a rapid synthesis method, aliovalent doping of the Li^+ site with Ca^{2+} or Al^{3+} generates vacancies which improve Li^+ diffusion and conductivity. This is confirmed by pulsed-field gradient (PFG)-NMR and impedance spectroscopy. The "super Cl-rich" material with overall composition $Li_{5.35}Ca_{0.1}PS_{4.5}Cl_{1.55}$ exhibits a superionic room temperature conductivity of 10.2 mS·cm^{-1} in the cold-pressed state and an exceptional diffusivity of 1.21×10^{-11} m^2/s. The presence of the aliovalent dopant on the Li sites in the cubic structure is supported by ^7Li magic-angle spinning NMR and Rietveld refinement of neutron powder diffraction data. Importantly, we also probed the impact of mechanical modification on grain boundary diffusion in these sulfide electrolytes using PFG-NMR. Detection of a clear difference in activation energies between the powder and pellet-pressed versions indicates that the efficacy of particle-scale, materials engineering modifications of fast-diffusing solid electrolytes can be interrogated with the use of PFG-NMR. Our studies also show that analysis over a wide range of temperatures is often necessary for fitting PFG-NMR Arrhenius plots in order to be able to compare macroscopic measurements with transport coefficients indirectly extrapolated from microscopic measurements, such as NMR relaxometry techniques.
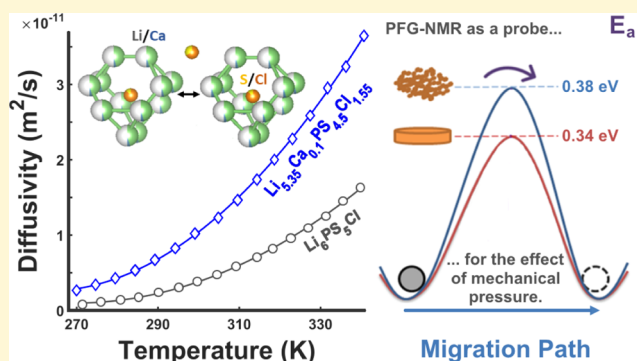
INTRODUCTION

Electric vehicles offer a means of integrating renewable energy into the transportation sector, while significantly reducing emissions. However, deeper intrusion of this technology into the market place requires improvement in the safety and energy density of battery platforms, with lithium all-solid-state batteries (ASSBs) being a notable potential avenue.[1,2] Li-ASSBs are attracting keen interest because of the possibility of enabling the use of a Li metal anode and replacement of the flammable organic electrolyte used in conventional Li-ion cells. The former enhances the energy density, and a leakage-free, nonflammable solid electrolyte poses fewer safety concerns. Solid-electrolyte implementation also benefits from less stringent packaging demands (leading to higher volumetric energy density) and relies on exclusive mobility of Li cations in the electrolyte, consequently avoiding the concentration gradients observed in liquid electrolytes.[3,4]

Despite these putative advantages of ASSBs, a long way to large-scale commercialization remains. One challenge lies in the development of ultrahigh conductive solid electrolytes (in the range of 10 mS·cm^{-1}) coupled with good electrochemical stability. This has motivated the escalating quest for new materials which can compete with the performance of current liquid electrolytes.[5] Extensive research has led to the development of Li-ion conducting oxides (including perovskites,[6] antiperovskites,[7] garnets,[8] NASICON,[9] and LiSICON[10]); solid polymer electrolytes (SPEs);[11] and sulfides such as $Li_7P_3S_{11}$,[12] $Li_{3.25}Ge_{0.25}P_{0.75}S_4$,[13] $Li_{10}GeP_2S_{12}$ (LGPS),[14] $Li_2S-P_2S_5$,[15] $Li_{9.54}Si_{1.74}P_{1.44}S_{11.7}Cl_{0.3}$,[16] and Li-argyrodites.[17] SPEs are soft and can accommodate volume changes of the electrodes, but they possess a low ionic conductivity (10^{-8} to 10^{-6} S·cm^{-1}) at room temperature because of restricted local polymer chain motion.[11,18] Thiophosphates, on the other hand, offer high ionic conductivity, and they are ductile, which is a crucial factor for making good contact between solid particles for cold-pressed pellets or membranes with no sintering necessary. In this class, Li-argyrodites such as Li_6PS_5Cl are particularly promising candidates for ASSBs because of their ease of preparation, comparatively inexpensive

precursors, high ionic conductivities, and reported electrochemical stability.[19] This material class has been utilized as solid electrolytes with various cathode and anode materials in several innovative ASSB cells.[20−24]

The argyrodite family spans a wide general composition $A_{(12-n-x)/m}^{m+}B^{n+}L_{6-x}^{2-}M_x^-$ (A = Ag$^+$, Cu$^+$, Li$^+$, etc.; B = Ga^{3+}, Si^{4+}, and P^{5+}; L = S, Se, and Te; and M = Cl, Br, and I).[25] The cubic Li$_6$PS$_5$X (X = Cl, Br, and I) structure within this group comprises PS$_4^{3-}$ tetrahedra and isolated S^{2-}/X$^-$ and Li$^+$ ions in the lattice.[17] The Li sites form localized cages (Frank−Kasper polyhedra), within and between which various Li$^+$-ion jumps are feasible: intracage (48h−48h) hops, doublet hops (48h−24g−48h), and intercage hops.[26] Each cage hosts twelve 48h sites, which are approximately half occupied. Fast ion conductivity is exhibited by the X = Cl and Br phases, where S^{2-} and X$^-$ are disordered on two crystallographic positions (4a, 4c) in the cubic lattice. Even higher conductivity is obtained for Li$_{6-x}$PS$_{5-x}$X$_{x+1}$ phases, where the substitution of additional Cl$^-$ in the lattice on the two (4a, 4c Wyckoff) mixed S^{2-}/Cl$^-$ sites induces vacancies on the Li sites.[27]

Several theoretical and experimental studies on anion site substitution have been reported for this class of materials[26,28−34] and for cation substitution on the P site.[35−39] Meanwhile, cation substitution on the Li site and dual modification are areas that have not been well explored. Schneider *et al.* recently reported stabilization of high-temperature Li$_7$PS$_6$ by doping the Li site with iron to form Li$_6$Fe$_{0.5}$PS$_6$, which exhibits a relatively low ionic conductivity of 1.4×10^{-4} S·cm^{-1}.[40] Other groups claimed partial substitution of Al^{3+}/B^{3+} on the Li site for Li$_6$PS$_5$X (X = Cl and Br) on the basis of X-ray diffraction (XRD) refinements where Li$_{5.4}$Al$_{0.2}$PS$_5$Br exhibits a room-temperature conductivity of 2.4 mS·cm^{-1}.[41] Another study showed that Y^{3+}-doped Li$_6$PS$_5$Cl exhibits a negligible difference in room-temperature ionic conductivity *vis a vis* Li$_6$PS$_5$Cl and that YCl$_3$ is exsolved in the grain boundary.[42] A patent application covers compositions in the argyrodite lattice derived by substitution of monovalent alkali cations for Li$^+$, such as Na$^+$ and K$^+$.[43] While the reason for the substitution of a monovalent ion is not clear, substitution of a divalent cation with a similar radius to Li$^+$, such as Mg^{2+} or Ca^{2+}, is strongly motivated by the concomitant increase in vacancy concentration on the lithium site. As we report here, it is responsible for more than a doubling in the ionic conductivity compared to the parent phase when coupled with a small increase in the Cl$^-$/S^{2-} ratio. We probed the structure and ionic transport properties *via* powder neutron diffraction (PND), electrochemical impedance spectroscopy (EIS), ^{7}Li and ^{31}P magic-angle spinning (MAS), and pulsed-field gradient (PFG) NMR. PFG-NMR has found recent application in several solid-state electrolyte systems,[27,44−47] as diffusion rates in these materials have increased to the point of accessibility for the technique. It requires relaxation to be sufficiently slow to encode and refocus a gradient phase, as well as maintain a signal for long enough that even slow diffusive motion is detectable. Importantly, we use PFG-NMR to examine the influence of mechanical compression of the material on the measured lithium-ion transport because it is important to understand this impact, given the advantage of high solid electrolyte ductility with regard to device fabrication. Our study helps develop a better understanding of the fundamental structure−property interplays that govern the ionic transport and lead to enhanced performance in this class of materials.

■ EXPERIMENTAL METHODS

Materials Synthesis and Characterization. In the past, a majority of the Li-argyrodite solid electrolytes have been synthesized by extensive mechanical milling of the solid precursors followed by long heat treatment.[21,48−50] More recently, a direct solid-state route by Wagemaker *et al.* was developed that utilized a short ball milling step with a 10 h heat treatment.[51] Recently, Zeier *et al.* have prepared their highly conductive argyrodite (Li$_{6+x}$P$_{1-x}$Ge$_x$S$_5$I) *via* hand grinding, followed by a 2-week heat treatment.[52] In our synthesis procedure, all the argyrodite compositions Li$_{6-2y}$Ca$_y$PS$_5$Cl (y = 0, 0.05, 0.1, 0.15, 0.2), Li$_{6-x-2y}$Ca$_y$PS$_{5-x}$Cl$_{1+x}$ (x = 0.25, y = 0.1; x = 0.25, y = 0.15; x = 0.375, y = 0.1; x = 0.5, y = 0.1), Li$_{6.1-x-2y}$Ca$_y$PS$_{5.05-x}$Cl$_{1+x}$ (x = 0.55, y = 0.1), and Li$_{6-x-3y}$M$_y$PS$_{5-x}$Cl$_{1+x}$ (M: Al or Ga) (y = 0.05; y = 0.1; y = 0.15; y = 0.2; x = 0.15, y = 0.1; x = 0.25, y = 0.1; x = 0.35, y = 0.1; x = 0.25, y = 0.2) were prepared by minimal grinding of the precursors (15 min), followed by a short heat treatment (5 h) at 550 °C. In each case, the mixture was pelletized, and the pellets were placed in a glassy carbon crucible and sealed in a quartz ampoule. Further details are given in the Supporting Information.

X-ray and Neutron Diffraction Measurements. The air-sensitive products were ground and sealed in a 0.3 mm diameter quartz capillary for powder XRD measurements. The XRD patterns were measured on a PANalytical Empyrean X-ray diffractometer using Cu Kα radiation (1.5406 Å). Time-of-flight (TOF) neutron diffraction data were collected on POWGEN at the Spallation Neutron Source at the Oak Ridge National Laboratory (center λ: 1.5 Å, d-spacing over the range of 0.50097−13.0087 AÅ) at ambient temperature. The program GSAS II was used for Rietveld refinement, and the Li$_6$PS$_5$Cl structure in the space group $F\bar{4}3m$ was used as a starting point for the refinement. The P and S occupancies on the 4b and 16e sites were fixed at their stoichiometric values. The atomic coordinates and atomic displacement parameters (U_{iso}) were restrained to be the same for the shared sites S1 and Cl1 (and for S2 and Cl2). The sum of occupancies was set to one for the shared sites [Occ(S1) + Occ(Cl1) = 1 and Occ(S2) + Occ(Cl2) = 1], and the atomic coordinates were restrained to be the same for Li and Ca on the 48h site. All other parameters were subsequently refined.

NMR Spectroscopy. High-field, fast MAS NMR was performed with a 1.9 mm probe on a Bruker 850 MHz HD spectrometer in a zirconia rotor, with ^{7}Li possessing a 330 MHz Larmor frequency at the 20 T field strength. A 30 kHz MAS rate was employed for all samples, and a 3.5 μs, 110 W excitation pulse generated the spectra. Referencing of the ^{7}Li signal was nominally to 1 M LiCl(aq), but it was found with previous studies[27] that to trace LiCl(s) impurity stemming from the argyrodites themselves was more reliable. Fast MAS for ^{31}P was also conducted for the super Cl-rich composition, Li$_{5.35}$Ca$_{0.10}$PS$_{4.50}$Cl$_{1.55}$, using a 1.9 mm zirconia rotor with a 30 kHz MAS rate on the Bruker 850 MHz HD spectrometer (^{31}P Larmor frequency of 343 MHz), and signals were referenced to 85% H$_3$PO$_4$ in a capillary standard.

Diffusion measurements were conducted using the PFG NMR technique with a Bruker Avance III 300 MHz spectrometer (7.0 T; ^{7}Li has a Larmor frequency of 117 MHz at this field strength) and a Diff50 gradient probe with a 5 mm ^{7}Li coil insert. Samples were placed in a Shigemi tube with a packing depth of 3−4 mm in an Ar-filled glovebox, and the tube was sealed with parafilm. The sample plug in the Shigemi tube was aligned with the center of the gradient coil using a standard ^{7}Li frequency-encoding magnetic resonance imaging.

Further details are given in the Supporting Information.

Scanning Electron Microscopy and Energy-Dispersive X-ray Analysis. A Zeiss Leo 1530 field emission scanning electron microscope [with an energy-dispersive X-ray (EDX) detector] was utilized for microstructural observation of the materials and elemental analysis. As the materials were not stable under prolonged electron beam illumination, an acceleration voltage of 15 kV with an acquisition time of 1 min was used for EDX measurements.

Electrochemical Impedance Spectroscopy. EIS was employed to obtain the ionic conductivities. Powder samples were sandwiched

between two stainless steel (SS) rods (diameter of 10 mm) and cold-pressed at 2 tons by a uniaxial hydraulic press to give pellets between 0.5 and 1.1 mm thick. EIS measurements were carried out by sandwiching the pellets between two indium foils at 100 mV, in the frequency range of 1 MHz to 100 mHz at 298 K using a VMP3 potentiostat/galvanostat (BioLogic). For temperature-dependent conductivity measurements, impedance spectra were recorded in the frequency range of 35 MHz to 100 mHz with the MTZ-35 impedance analyzer (BioLogic) controlled by the MT-Lab (BioLogic) software from 298 to 338 K at 5 K intervals. The EIS measurement for $x = 0.5$, $y = 0.1$ was performed at 273 K by immersing the sealed EIS cell in a cooling bath and waiting until equilibrium was achieved. Data analysis was performed using the EC-Lab software, and the activation energy was determined from the slope of the Arrhenius plot.

RESULTS AND DISCUSSION

Compositions Varying Only in Ca Content. Targeted compositions $Li_{6-2y}Ca_yPS_5Cl$ ($y = 0$, 0.05, 0.1, and 0.15) were prepared. The XRD patterns for ($y = 0$, 0.1, 0.15) are shown in Figure S1. These argyrodites show a minute fraction of impurities (<1.5 wt %; see Figures S2a and 1−3 below for
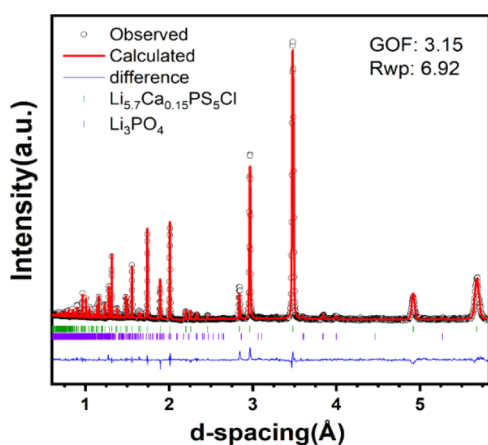

Figure 1. TOF neutron powder diffraction pattern of the targeted $Li_{5.7}Ca_{0.15}PS_5Cl$ after heat treatment at 550 °C for 5 h. Ticks for the minority Li_3PO_4 phase (<1.5 wt %) are in purple.

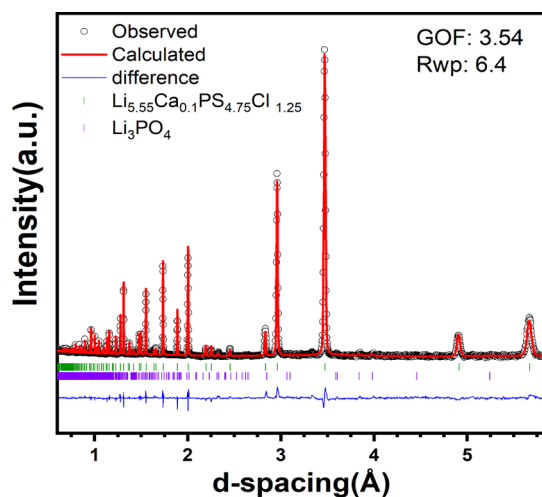**Figure 2.** TOF neutron powder diffraction pattern of $Li_{5.55}Ca_{0.1}PS_{4.75}Cl_{1.25}$. Bragg reflections are shown in green; ticks for the minority Li_3PO_4 phase (0.63 wt %) are in purple.

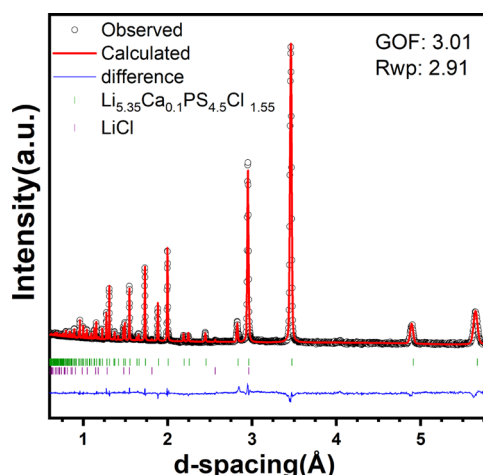**Figure 3.** TOF neutron powder diffraction pattern of $Li_{5.35}Ca_{0.1}PS_{4.5}Cl_{1.55}$ after heat treatment at 550 °C for 5 h. Ticks for the minority LiCl phase (0.6 wt %) are in purple.

quantitative Rietveld refinements of the XRD and PND data, respectively) that are not likely to impact the ionic conductivity. Attempts to increase the Ca^{2+} fraction to $y = 0.2$ led to the rise of Li_3PS_4 and CaP_4O_{11} impurities (see XRD pattern in Figure S3) and a decrease in the ionic conductivity, indicating that $y = 0.15$ is the limit of solid solubility.

In order to better understand the structural influence of Ca^{2+} doping on the argyrodite, Rietveld refinement against the neutron diffraction pattern was carried out for $y = 0.15$ ($Li_{5.7}Ca_{0.15}PS_5Cl$; Figure 1) in the cubic space group $F\bar{4}3m$, yielding reasonable occupancy values that were in accord with the targeted stoichiometry. Because of the low fraction of Ca^{2+} in the lattice, U_{iso} for Ca (0.05 A$Å^2$) was not refined and was set to be about half that of Li (assuming that a divalent cation will have a smaller atomic displacement parameter on the same site because of its divalent nature and larger size). Performing the refinement without fixing U_{iso} for Ca^{2+} or with smaller U_{iso} values (e.g., 0.04 A$Å^2$),[53] which was reported for Ca^{2+} dopants in other cubic thiophosphates, did not yield meaningful occupancies. We recognize that the accuracy of the refined occupancy of Ca^{2+} could be compromised by our approach; nonetheless, the refined composition ($Li_{5.71}Ca_{0.15}PS_{4.95}Cl$) is almost identical to the targeted stoichiometry ($Li_{5.70}Ca_{0.15}PS_5Cl$). The refinement of these room temperature data (Table 1) reveals that both Li^+ and Ca^{2+} ions partially occupy the 48h site, and neither are present on the 24g site. In this Li vacancy-rich material, as in the other Ca-substituted compositions (Figures 2 and 3 discussed below), we do not observe occupation on additional sites in the lattice that were recently revealed by low-temperature neutron diffraction studies of our "Li-stuffed" argyrodite $Li_{6+x}M_xSb_{1-x}S_5I$[54] and by Zeier's group for Li_6PS_5X (X = Cl, Br).[55] The site disorder (ratio of Cl^-/S^{2-} on the 4c site, 62.8%) is almost the same as in the parent phase (61.5%). EDX analysis confirmed the homogeneity within the material and showed elemental ratios that were in accord with the theoretical values. Selected examples of the normalized ratios obtained from EDX are given in Table S1. For $y = 0.1$ and $y = 0.15$, the Ca/P/Cl ratios are 0.10:1.01:1.00 and 0.16:0.99:1.00, respectively.

Compositions Varying in Both Ca and Cl Contents. Targeted compositions $Li_{6-x-2y}Ca_yPS_{5-x}Cl_{1+x}$ ($x = 0.25$, $y = 0.1$; $x = 0.25$, $y = 0.15$; $x = 0.375$, $y = 0.1$; and $x = 0.5$, $y = 0.1$)

Table 1. Atomic Coordinates, Occupation Factors, and Isotropic Displacement Parameters of $Li_{5.7}Ca_{0.15}PS_5Cl$ Obtained from the Rietveld Refinement of Neutron TOF Data at Room Temperature [Space Group $F\bar{4}3m$; $a = 9.8414(1)$ Å and Volume = 953.20(2) Å^3] That Yield a Refined Composition of $Li_{5.71}Ca_{0.15}PS_{4.95}Cl$

atom	Wyckoff site	x	y	z	SOF	U_{iso} (AÅ^2)
Li	48h	0.3116	0.0234	0.6885	0.476(14)	0.084(4)
Ca	48h	0.3116	0.0234	0.6885	0.0125(30)	0.05
Cl1	4a	0	0	0	0.420(9)	0.024(1)
Cl2	4c	1/4	1/4	1/4	0.628(11)	0.033(1)
P1	4b	0	0	0.5	1	0.025(1)
S1	4a	0	0	0	0.580(9)	0.024(1)
S2	4c	1/4	1/4	1/4	0.372(11)	0.033(1)
S3	16e	0.1189	−0.1189	0.6189	1	0.040(1)

Table 2. Atomic Coordinates, Occupation Factors, and Isotropic Displacement Parameters of $Li_{5.55}Ca_{0.1}PS_{4.75}Cl_{1.25}$ Obtained from Rietveld Refinement of Neutron TOF Data (Space Group $F\bar{4}3m$) $a = 9.8222(1)$ AÅ and Volume = 947.59(2) Å^{3a}

atom	Wyckoff site	x	y	z	SOF	U_{iso} (AÅ^2)
Li	48h	0.3143(15)	0.0212(9)	0.6858(15)	0.463(3)	0.075
Ca	48h	0.3143(15)	0.0212(9)	0.6858(15)	0.008(3)	0.05
Cl1	4a	0	0	0	0.536(15)	0.028(1)
Cl2	4c	1/4	1/4	1/4	0.738(15)	0.033(1)
P1	4b	0	0	0.5	1	0.030(1)
S1	4a	0	0	0	0.464(15)	0.028(1)
S2	4c	1/4	1/4	1/4	0.262(15)	0.033(1)
S3	16e	0.120	−0.120	0.620	1	0.049(1)

^{a}The calculated composition $Li_{5.56}Ca_{0.10}PS_{4.73}Cl_{1.27}$ is close to the targeted one.

Table 3. Atomic Coordinates, Occupation Factors, and Isotropic Displacement Parameters of $Li_{5.35}Ca_{0.1}PS_{4.5}Cl_{1.55}$ Obtained from Rietveld Refinement of Neutron TOF Data (Space Group $F\bar{4}3m$) $a = 9.7898(1)$ AÅ and Volume = 938.24(3) Å^{3a}

atom	Wyckoff site	x	y	z	SOF	U_{iso} (AÅ^2)
Li	48h	0.3174(8)	0.0227(10)	0.6827(8)	0.447(3)	0.075
Ca	48h	0.3174(8)	0.0227(10)	0.6827(8)	0.007(3)	0.05
Cl1	4a	0	0	1	0.668(19)	0.020(1)
Cl2	4c	1/4	1/4	3/4	0.867(17)	0.031(1)
P1	4b	0	0	0.5	1	0.030(1)
S1	4a	0	0	1	0.332(19)	0.020(1)
S2	4c	1/4	1/4	3/4	0.133(15)	0.031(1)
S3	16e	0.1200	−0.1200	0.6200	1	0.048(1)

^{a}The calculated composition $Li_{5.36}Ca_{0.08}PS_{4.47}Cl_{1.54}$ is very close to the target.

were prepared. The XRD patterns of ($x = 0.25$, $y = 0.1$) and ($x = 0.375$, $y = 0.1$) are presented in Figure S1, indicating that the materials are essentially pure single phases. The composition was confirmed by refinements against the XRD data for ($x = 0.375$, $y = 0.1$; Figure S2b) and ($x = 0.5$, $y = 0.1$; Figure S4, Table S2) and against the PND data for $x = 0.25$, $y = 0.1$ (Figure 2) that all revealed ≤2.7 wt % impurities. However, additional Ca substitution to target a nominal composition of $Li_{5.45}Ca_{0.15}PS_{4.75}Cl_{1.25}$ led to a notable fraction of secondary phases, which had an undesirable impact on the ionic conductivity. We conclude that the Cl-rich argyrodites cannot sustain as high a degree of Ca substitution, likely owing to vacancy limitations on the 48h site. The local structure of $x = 0.5$, $y = 0.10$ was explored with Raman, showing only the PS_4^{3-} moiety with no evidence of P_2S_6 (Figure S5). The EDX for this phase yielded a Ca/P/Cl ratio of 0.10:1.00:1.48.

Rietveld refinement of $x = 0.25$, $y = 0.1$ was performed against the neutron data (Figure 2), where the U_{iso} values for Li and Ca on the 48h site were fixed (see Experimental Methods). The results of the refinement presented in Table 2 reveal a composition of $Li_{5.56}Ca_{0.10}PS_{4.73}Cl_{1.27}$ that is very close

to the targeted $Li_{5.55}Ca_{0.1}PS_{4.75}Cl_{1.25}$. The additional Cl is distributed equally on the 4a and 4c sites.

Rietveld refinement of the "super Cl-rich" $x = 0.55$, $y = 0.1$ was similarly performed against neutron diffraction data (Figure 3), where the U_{iso} values for Li and Ca on the 48h site were fixed (see Experimental Methods). The results of the Rietveld refinement are presented in Table 3 and show a refined composition of $Li_{5.36}Ca_{0.08}PS_{4.47}Cl_{1.54}$ that is almost identical to the targeted $Li_{5.35}Ca_{0.1}PS_{4.5}Cl_{1.55}$. While the diffraction pattern of this "super Cl-rich" material appears to be single-phase, its ^7Li NMR spectrum reveals the presence of two closely related argyrodite-type phases, as discussed below (see the NMR Spectroscopy section).

Compositions Containing Tri- and Tetravalent Cations. Other aliovalent dopants on the Li site were also explored, including but not limited to trivalent Ga^{3+} and Al^{3+} and tetravalent Zr^{4+} and Si^{4+}. Different factors such as the size of the cation, mobility, charge, cost, and elemental abundance were considered. Ge substitution on the P site was recently reported, yielding extremely high conductivity, but this presents limitations in both cost and stability.[52] Owing to

the smaller size of Al^{3+} (0.535 Å) and Ga^{3+} (0.620 Å) cations compared to Li^+ (0.76 Å), only small fractions of the dopant could be incorporated ($y = 0.1$); selected XRD patterns/Rietveld refinements (Figures S6 and S7), along with EDX data, (Table S3) are provided. Attempts to synthesize phase pure $Li_{6-3y}M_yPS_5Cl$ (M = Al and Ga) at $y > 0.15$ were unsuccessful and led to significant Li_3PS_4 and lithium thiogallate ($LiGaS_2$) impurities, respectively. Si^{4+} or Zr^{4+} doping was not feasible. Given that the Ca-argyrodite-prepared materials exhibited the most promising results in terms of purity and conductivity (discussed later in the Transport Properties of the Ca-Doped Compositions section) at higher doping levels, we focused the ^7Li NMR investigations on this set of materials which utilize earth-abundant elements Ca, P, and S.[56]

^7Li MAS NMR Probe of Ca^{2+} Doping. The presence of Ca^{2+} in the vicinity of Li^+ was also established by the appearance of a small secondary peak in the ^7Li MAS NMR measurements for several Ca^{2+}-containing compositions (Figure 4), along with the expected main resonance. Deconvolution of the lineshapes for $y = 0.1$, $y = 0.15$, and ($x = 0.25$, $y = 0.1$), for which the secondary peak was not
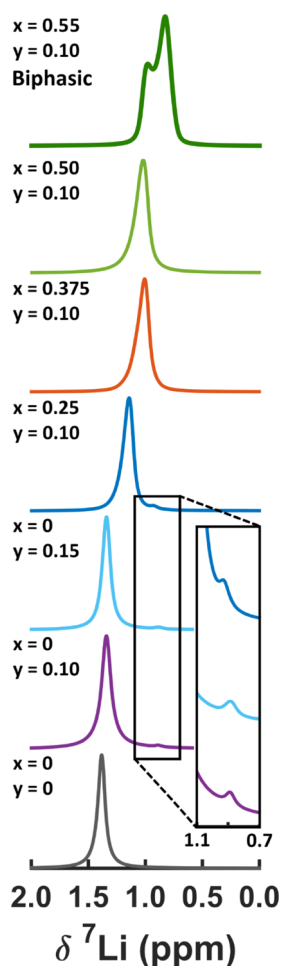

Figure 4. Stack plots of ^7Li MAS spectra for the y-series and dual-modified series, demonstrating the strong chlorine-enrichment shift trend, and no major change in the chemical shift associated with Ca^{2+} doping. The inset reveals the secondary peak associated with the Ca^{2+} dopant that modifies the local electronic environment of a subset of the Li ions.

obscured by the larger, halide enrichment-induced chemical shift trend,[27] yielded peak areas with ratios corresponding to the Li^+/Ca^{2+} stoichiometric ratio in each case (Figure S8). Additionally, ^7Li nuclear Overhauser effect spectroscopy (NOESY), while not quantitative in this case owing to the difficulty in deconvoluting overlapping spectral volumes, indicates that lithium species generating these secondary peaks are in close proximity to those producing the primary peaks. That is, they are within the same phase and not due to a contaminant impurity because the cross peaks in a NOESY experiment can only form directly via chemical exchange or because of short-range homonuclear dipolar coupling (i.e., spin diffusion).[57] The cross peaks in these NOESY spectra indicate that the Li ions corresponding to the two peaks are more than likely undergoing chemical exchange, given the short mixing times involved (Figure S9). Variable-temperature experiments to test the thermal activation of the cross-peak onset were not attempted. Further to this point, the secondary peak for the much faster diffusing ($x = 0.25$, $y = 0.1$) composition is closer to the main resonance than it is for the $y = 0.1$ and $y = 0.15$ compositions, indicating a greater degree of averaging of the signals on the NMR timescale.

For several nominally targeted ($x = 0.5$, $y = 0.1$) compositions, we observed more than one main peak in the ^7Li MAS NMR spectrum (Figures 4 and S10). Although there was no indication of more than one significant phase in the XRD or PND pattern, these materials exhibited higher diffusivity. This prompted us to increase the Cl content further and target the composition $Li_{5.35}Ca_{0.1}PS_{4.5}Cl_{1.55}$. This "super Cl-rich" material appears to be single-phase by neutron diffraction (Figure 3), but its biphasic nature is evidenced by its ^7Li MAS NMR spectrum (Figure 4, upper trace in dark green), which exhibits two very well-resolved peaks. The peak at 0.98 ppm is consistent with the phase where $x \simeq 0.5$, whereas the new narrow peak at 0.83 ppm that is shifted to a much lower frequency environment is indicative of a more chlorine-rich argyrodite. This peak does not correspond to LiCl, which appears at −1.2 ppm as a solid[27] and was only observed in trace amounts in the full spectra of Figure 4 (not shown). Semiquantitative analysis based on the 1:2 area of the two peaks in the spectrum (derived from curve deconvolution) and the overall targeted stoichiometry suggest a composition of $x \sim 0.63$ for the new argyrodite at 0.83 ppm. The jump to a much lower frequency (vis a vis the $x = 0.50$ composition) indicates that the lithium ions in this argyrodite (which may form nanodomains not resolvable in the PND pattern) exhibit a unique electronic environment that is more highly surrounded by chloride anions. The ^{31}P MAS NMR for this material also exhibits a series of shifts with cascading intensities, indicative of progressively higher amounts of Cl^- substitution in the surrounding anion shells (Figure S11).

Physical and Electrochemical Properties. The relative density of all the cold-pressed pellets was 91 ± 0.8 g·cm^{-3} (Table S4). This value was calculated using the sample geometry and mass compared to the theoretical density of the argyrodite. The morphology of the microcrystalline material obtained by scanning electron microscopy (SEM, Figure 5a) reveals that there is a distribution in the size of the particles (predominantly 0.5 to 5 μm), and Ca substitution does not influence the dominant grain size range (Figure 5b).

Evaluation of the electrochemical stability of the Ca-doped electrolyte via cyclic voltammetry provides a initial assessment of its robustness against lithium metal. For example, Jung et al.
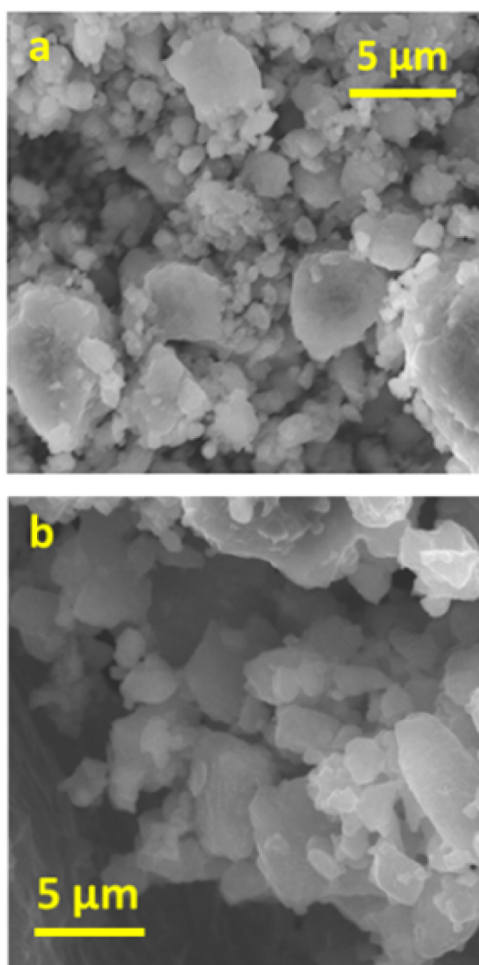
Figure 5. SEM images of (a) y = 0.1 x = 0, (550 °C, 5 h) and (b) y = 0.15 x = 0, (550 °C, 5 h).

Figure 6. (a) Cyclic voltammogram of the SS/y = 0.1 (x = 0)/Li cell with a scan rate of 1 mV s^{-1} in the voltage window of 5.0 to −0.1 V; the inset shows the magnified view in the voltage range of 0.4 to −0.1 V. (b) DC polarization curve for y = 0.15 (x = 0) at 0.25 V (black), 0.5 V (red), and 0.75 V (blue) (cold-pressed at 2 tons and 300 K).

carried out cyclic voltammetry to show that despite the ultrahigh conductivity of LGPS, it exhibits poor electrochemical stability in the voltage range below ~1 V (vs Li/Li$^+$), as Ge is easily reduced.[58] We recorded the cyclic voltammograms of the SS/y = 0.1 (x = 0)/Li cell in a voltage window of 5.0 to −0.1 V at a scan rate of 1 mV s^{-1} at 300 K (illustrated in Figure 6a), which are similar conditions previously reported for y = 0.[19] Good, reversible stripping and plating behavior was observed. The materials also exhibit low electronic conductivity; the DC polarization curve of a representative sample (y = 0.15, σ_e = 5 × 10^{-9} S·cm^{-1}) is demonstrated in Figure 6b. Thus, the combination of good stability and low electronic conductivity makes the substituted argyrodite materials favorable as a solid electrolyte.

Transport Properties of the Ca-Doped Compositions. Temperature-dependent EIS and PFG-NMR measurements were carried out to assess changes to the ion transport as a result of Ca^{2+} substitution in selected standard and Cl-rich compositions. The corresponding impedance responses with the respective fits are shown in Figure 7a, and Arrhenius plots of all materials obtained from EIS are shown in Figures S12 and S13. Because the constant phase element (CPE)/resistor component is shifted to frequencies at room temperature that are too high to measure with the impedance analyzer, only the Warburg tail of the blocking electrodes was used for the fit. The impedance data at a low temperature (195 K) were fit
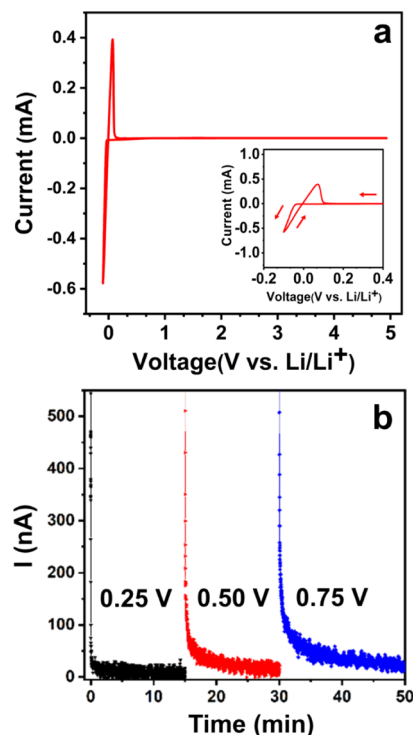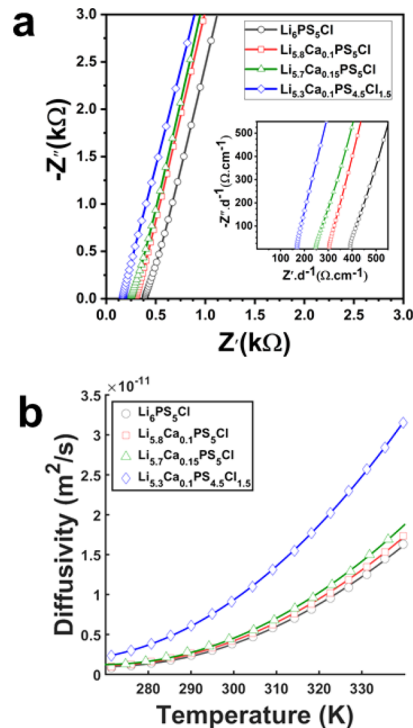

Figure 7. (a) Nyquist plots for y = 0, 0.1, 0.15, (x = 0) and y = 0.1, x = 0.5 at 298 K. The figure inset illustrates the enlarged view at high frequencies. For the sake of easy comparison, the impedance was normalized to the corresponding pellet thickness d (cm); (b) diffusivity plots for y = 0, 0.1, 0.15 (x = 0), y = 0.1, x = 0.5 from PFG NMR data.

with an equivalent circuit consisting of one parallel CPE/resistor in series with a CPE, representing the blocking electrodes. Bulk and grain boundary contributions could not be deconvoluted, but the α value of 0.9 denotes the ideality of the CPE (Figure S14 and Table S5). The ionic conductivities at room temperature and the activation energies (E_a) for compositions varying in both Ca and Cl contents are displayed in Table 4. The marriage of anion disorder and the presence of unoccupied neighboring sites for the mobile ion hops lead to excellent ionic conductivity up to 10 mS·cm^{-1}.

Table 4. Conductivity (σ at 298 K, for Cold-Pressed Pellets at 2 t) and Activation Energy (E_a) Values Obtained from EIS and PFG Arrhenius Plots for the Ca-Doped Argyrodites[a]

compositions	σ_{tot} [mS·cm^{-1}]	E_a (EIS) [eV] ± 0.01	E_a (PFG) [eV]
Li$_6$PS$_5$Cl (pristine)	3.1	0.34	0.35(1)
Li$_{5.9}$Ca$_{0.05}$PS$_5$Cl	3.5		
Li$_{5.8}$Ca$_{0.1}$PS$_5$Cl	4.3	0.35	0.337(4)
Li$_{5.7}$Ca$_{0.15}$PS$_5$Cl	5.2	0.34	0.334(3)
Li$_{5.6}$Ca$_{0.2}$PS$_5$Cl	3.4		
Li$_{5.55}$Ca$_{0.1}$PS$_{4.75}$Cl$_{1.25}$	6.8	0.33	0.317(6)
Li$_{5.45}$Ca$_{0.15}$PS$_{4.75}$Cl$_{1.25}$	6.1		
Li$_{5.425}$Ca$_{0.1}$PS$_{4.625}$Cl$_{1.375}$	7.2	0.31	0.307(7)
Li$_{5.3}$Ca$_{0.1}$PS$_{4.5}$Cl$_{1.5}$	7.7	0.31	0.302(5)
Li$_{5.35}$Ca$_{0.1}$PS$_{4.5}$Cl$_{1.55}$-pellet	**10.2**	**0.30**	**0.287(4)**
Li$_{5.35}$Ca$_{0.1}$PS$_{4.5}$Cl$_{1.55}$-powder			0.301(4)

[a]See Table S6 for analysis details. Errors in the PFG measurements are derived from the linear regression fit of the Arrhenius plots.

The site disorder arises because Cl$^-$ ions share two sites (4a and 4c) with S^{2-}, which alters the energy landscape for Li-ion diffusion.[33] For Li$_{6-2y}$Ca$_y$PS$_5$Cl, the step-wise introduction of Ca in the Li site is accompanied by a gradual increase in vacancy concentration, which is the main contributor to the enhancement in the conductivity, given that the disorder is not significantly changed *vis a vis* Li$_6$PS$_5$Cl. The effect of Ca^{2+} incorporation on the intracage or doublet jumps should be negligible at this small level of doping (one Ca per ~10 and ~6 cages for y = 0.1, y = 0.15, respectively). It is the long-range transport between the cages (intercage), which dictates the macroscopic conductivity in Li argyrodites, as demonstrated by *ab initio* molecular dynamics simulations. These studies showed that the intercage jump rate has the lowest jump frequency of all and will hence limit macroscopic diffusion. For example, in the case of Li$_6$PS$_5$Cl, the jump rates are 0.73, 17.78, and 21.58 ($\times 10^{10}$ s^{-1}) for intercage, intracage, and doublet jumps, respectively.[33] The fact that Ca^{2+} does not disrupt transport is further supported by the activation energies of the solely Ca^{2+}-substituted phases (Table 4), which are effectively the same as Li$_6$PS$_5$Cl. Regarding the argyrodites with trivalent dopants, selected conductivity and extracted impedance analysis values are demonstrated in Table S7, among which x = 0.1 (Li$_{5.45}$Al$_{0.1}$PS$_{4.75}$Cl$_{1.25}$) exhibited the highest ionic conductivity of the compositions (5.7 mS·cm^{-1}), which is close to that of its Ca^{2+} counterpart, Li$_{5.55}$Ca$_{0.1}$PS$_{4.75}$Cl$_{1.25}$ (σ = 6.8 mS·cm^{-1}).

Hence, doping with an aliovalent cation introduces Li vacancies and these increase the Li-ion diffusivity, as demonstrated in Figure 7b, owing to a lower E_a value for defect formation. Room-temperature Li$^+$ diffusivities exhibited

by the y = 0.1 and y = 0.15 phases are 4.15 × 10^{-12} and 4.44 × 10^{-12} m^2/s, respectively, reflecting a respective 8 and 15% increase compared with 3.85 × 10^{-12} m^2/s for y = 0 (parent phase),. The dual-modified argyrodite x = 0.5, y = 0.1 exhibited an even higher diffusivity of 9.10 × 10^{-12} m^2/s, which is about 2.5 times that of the parent phase, but lower than that of the solely Cl-enriched phase (Li$_{5.5}$PS$_{4.5}$Cl$_{1.5}$).[27] In contrast, the diffusivity of the super Cl-rich Li$_{5.35}$Ca$_{0.1}$PS$_{4.5}$Cl$_{1.55}$ composition is 33% higher than x = 0.5, y = 0.1 with a remarkable value of 1.21 × 10^{-11} m^2/s. In Li$_{6-x-2y}$Ca$_y$PS$_{5-x}$Cl$_{1+x}$, simultaneous substitution of the Li cations and modification of anions yield additional vacancies that contract the lattice to result in a progressive decrease in the intercage hop distance with x, along with an increase in the site disorder (Figure 8, see PND tables
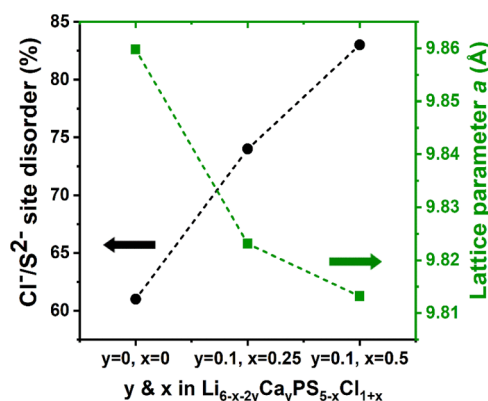

Figure 8. Site disorder and lattice parameter *vs* x for Li$_{6-x-2y}$Ca$_y$PS$_{5-x}$Cl$_{1+x}$.

given above and Table S2 in the Supporting Information). These factors, conjointly with the weakened electrostatic interactions between the mobile Li ions and surrounding framework anions (induced by substitution of divalent S^{2-} for monovalent Cl$^-$), are the key contributors to the high ionic conductivities for the dual-modified compositions, similar to what was found for the purely Cl-enriched argyrodites.[27] Ionic conductivities of the soft argyrodites can be further improved by hot pressing the powder or sintering and modifying the grain boundaries. Indeed, the effect of purely cold-pressing the material on the diffusivity constitutes a key component of this study and is described subsequently.

Activation energy is a factor that governs ionic conduction. For the Ca argyrodites, temperature-dependent conductivity measurements follow Arrhenius behavior where the lowest activation energy is exhibited by the super Cl-rich material x = 0.55, y = 0.1 (0.30 eV). The modified Arrhenius equation was applied to include a temperature-dependent pre-exponential: $\sigma T = \sigma_0 \exp(-E_a/k_b T)$, where σ is the temperature-dependent ionic conductivity, σ_0 is the prefactor, E_a is the activation energy for ion migration, and k_b and T represent their common meanings. E_a values were also obtained from ^{7}Li PFG-NMR and are in good accord with the values obtained from impedance spectroscopy, as compared in Table 4. It is important to also note that, for each dual-modified composition, the chemical shift was virtually identical to that of the equivalent x-only series previously studied.[27] Combined with the relatively small ^{7}Li chemical shift of the y-series relative to the parent phase Li$_6$PS$_5$Cl (see Figure 4), this suggests that the Ca^{2+} dopants do not significantly modify the electronic environment of Li$^+$ within the cages where Ca^{2+}

resides; their primary contribution to improving the transport is the introduction of excess vacancies to the Li^+ cage network, as illustrated in Figure 7b. The y-series activation energies are compared with those of the dual-modified series in Table 4.

This correlation is elaborated in Figure 9, which tracks the activation energy trends from both EIS and PFG-NMR, along
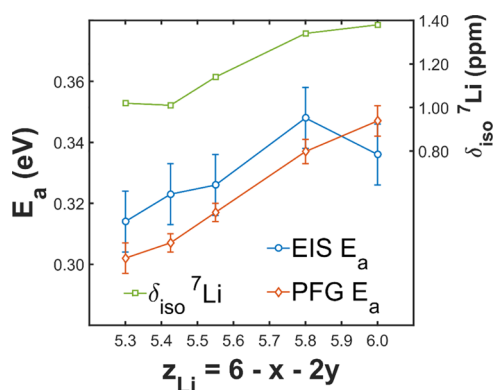

Figure 9. Correlation of activation energies from both EIS and PFG-NMR, as well as ^7Li isotropic chemical shift, with lithium vacancy concentration ($x + 2y$).

with the isotropic ^7Li chemical shift under MAS as a function of lithium stoichiometry, $z_{Li} = x + 2y$. This enables comparisons to be made between the y-series and the dual-modified series ($y = 0.1$). Increasing x lowers the ^7Li chemical shift toward a more ionic, "LiCl-like" environment, but this effect eventually saturates, indicating that there is a limit to which the substitution of S^{2-} sites with Cl^- can decrease Li^+ attraction to the anion framework. Nevertheless, the activation energy continues to decrease as x is increased, which stems from the impact of the additional vacancies on Li^+ sites. Conversely, the lack of shift decrease on going from $y = 0$ to $y = 0.1$ opposes the associated activation energy drop and can therefore be attributed strictly to the increased vacancy population. Figure 9 also demonstrates that the most significant lowering of the activation energy can be achieved by incorporating moderate Cl^- enrichment with a small amount of Ca^{2+} doping. The two effects act in concert to both lower the activation energy and boost the magnitudes of the conductivity and diffusivity to a greater amount than performing one or the other separately, at least when the solubility limit of the lattice with respect to either dopant is not exceeded.

Effect of Compression on Diffusivity Examined for the Super Cl-Rich Composition. Further insights into the magnitude of the activation energy changes were obtained by performing ^7Li PFG-NMR on both powder and pellet-pressed versions of the super Cl-rich material, $Li_{5.35}Ca_{0.10}PS_{4.50}Cl_{1.55}$. Over the temperature range of 243−358 K, the Arrhenius plots exhibit nonideal behavior, with curvature appearing in the lower temperature region of this range (Figure 10). This type of behavior has been previously observed in variable-temperature EIS measurements for $Li_{10}SnP_2S_{12}$,[59] where it was established as being a crossover from domination of grain-boundary contributions (in the lower temperature regime) to predominantly bulk grain contributions, by careful equivalent-circuit modeling of the Nyquist plots. The magnitude of activation energy difference for the super Cl-rich composition obtained by performing a two-component, limiting-slope fit of
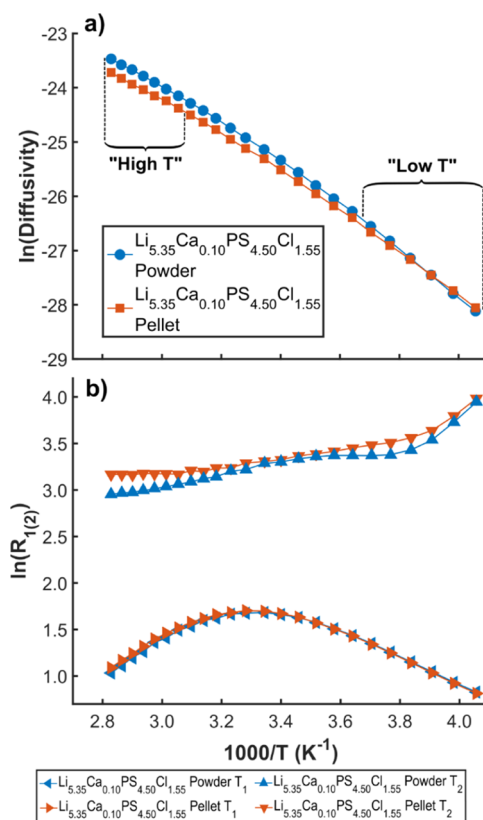

Figure 10. (a) Diffusivity Arrhenius plot from variable-temperature ^7Li PFG-NMR measurements on powdered and pressed-pellet versions of the super Cl-rich $Li_{5.35}Ca_{0.10}PS_{4.50}Cl_{1.55}$ material, showing nonideal Arrhenius behavior with a crossover in slopes from low to high temperature, which is significantly reduced in the pellet. (b) NMR relaxation rates compared between the powdered and pelletized $Li_{5.35}Ca_{0.10}PS_{4.50}Cl_{1.55}$. Note the presence of two inflection points in the T_2 curve, indicating the presence of two distinct motional correlation times.

the PFG-NMR Arrhenius plots (Figure 11) is evidently not as extreme as in $Li_{10}SnP_2S_{12}$. We found values for E_a(grain) versus E_a(grain boundary) of 0.26 to 0.38 eV, respectively, for uncompressed super Cl-rich $Li_{5.35}Ca_{0.10}PS_{4.50}Cl_{1.55}$, compared to a difference of 0.27 versus 0.60 eV for $Li_{10}SnP_2S_{12}$.[59] Of course, one can independently model the two contributions in EIS and disentangle them, but there is not a way to do that with PFG; one simply obtains the combined signal from all of the diffusion paths. Furthermore, the temperature range achievable with the PFG-NMR setup may not have been sufficiently low as to fully avoid fitting to some of the cross-over curvature between the grain- and grain boundary-dominated regimes. Nonetheless, the primary conclusion from comparing the activation energies between the powder and pellet-pressed samples is that in the "high temperature" regime (as defined by the range of temperatures fit to the upper limiting slope—see Figure 11), associated with the grain contribution, the Arrhenius slopes are essentially parallel. On the other hand, in the "low-temperature" regime, there is a distinct reduction in the slope between the pellet-pressed and powder materials, which can be attributed to the lowered difficulty of hops over grain dislocations in multicrystallite particles when the spatial extent of these gaps is reduced by the macroscopic compression of the material. The relative magnitudes of the activation energies for these regimes are
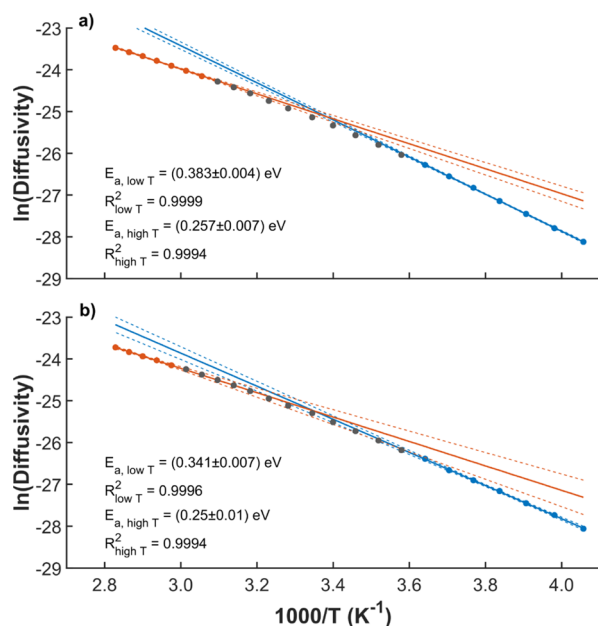
Figure 11. Two-component activation energy fits to the Arrhenius plots for the ^{7}Li PFG NMR data for the powdered (a) and pellet (b) versions of Li$_{5.35}$Ca$_{0.10}$PS$_{4.50}$Cl$_{1.55}$. The nonideal Arrhenius behavior is indicative of competing grain and grain boundary contributions to the overall lithium-ion transport, with the latter having greater influence at a lower temperature. That influence is reduced by the compression of the powder into a pellet (Figure 10).

summarized in Figure 12. It is to be noted that, for the sake of uniform comparison between the compositions, the PFG-
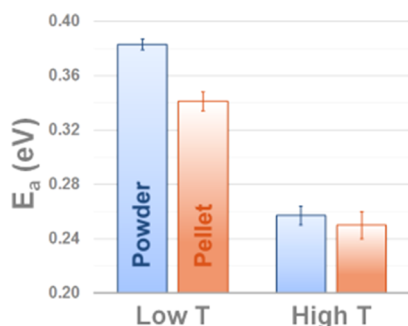

Figure 12. Comparison of the powder and pellet activation energies in the "low"- and "high-temperature" regions of the ^{7}Li PFG-NMR diffusivity Arrhenius plots for Li$_{5.35}$Ca$_{0.10}$PS$_{4.50}$Cl$_{1.55}$. (See Figure 11 for explicit delineations for the limiting slopes.) The high-T region is the same between samples and is associated with grain contributions, while the compression to form the pellet enhances the transport across grain dislocations in multicrystallite particles, which is the source of the lower activation energy in the pellet for the low-T region, and is associated with grain boundary contributions.

NMR activation energies for all compositions listed in Table 4 are single-component fits over the same temperature range of 268–343 K, though even within this more restricted temperature range, there is still evidence of a slight curvature in the Arrhenius plots (Figure S15).

As demonstrated in Figure 10, variable-temperature T_2 relaxation measurements clearly show the presence of two motional correlation times in the form of inflection points in the Eyring plot; one associated with the T_1 minimum and a separate one in the low-temperature flank, which has no

associated local minimum in the T_1 rate curve. The pairing of a T_1 minimum with an inflection point in the T_2 rate curve is a generic feature of the Bloembergen–Purcell–Pound relaxation theory, irrespective of the type of fluctuating interaction that is the source of the relaxation.[60] This buttresses the assignment in the diffusivity Arrhenius plot of two distinct regimes of motion, as opposed to a significant difference in the ion transport between the two lithium environments, which appear to exist in this super Cl-rich material (Figure S10). The same interaction must be driving the longitudinal relaxation in both (and is evidently not significantly modified by the mechanical compression), but there is an additional timescale purely associated with the motion that is influencing the T_2 rate curve in the lower-temperature region.

It is also interesting to note that T_2 is slightly reduced in the pelletized material relative to the powder at each temperature, and the diffusivity is also smaller, which again could be indicative of some extent of compression in the lattice within the grains itself. It is alternately possible that the reduced diffusivity in the compressed sample reflects restricted diffusion behavior within the grains that is influenced by grain geometry—and therefore altered by the compression—particularly as the grain-dominated region of the Arrhenius plot shows identical activation energies while the absolute diffusivities are smaller for the pellet sample. The mean diffusion paths for the measurements can be roughly estimated via the Einstein–Smoluchowski equation ($D^* = \langle(\Delta r)^2\rangle/2d\tau$ in the limit, where τ tends to infinity, Δr is the length of the mean diffusion path, and τ is the diffusion time for a process with dimensionality d)[61] and are of the order of a few microns (it is important to note that the roughness of this estimate stems from the neglect of interion correlations,[62] which will reduce the magnitude somewhat). This clearly places them in the regime between bulk-scale, macroscopic transport, and local ion hopping, but still greater than the average grain size. The complex interplay between grain morphology and the resulting effective diffusivity, particularly with the variable of compression pressure introduced, is therefore an intriguing direction for a future study and could potentially be interrogated by variable-Δ PFG-NMR measurements.

Nevertheless, the detection of this difference in activation energies between the powder and pellet-pressed versions of the super Cl-rich material indicates that the efficacy of particle-scale, materials engineering modifications of fast-diffusing solid electrolytes can be interrogated with the use of PFG-NMR. It further indicates that careful analysis over a wide range of temperatures is necessary for fitting PFG-NMR Arrhenius plots in these materials in order to be able to compare macroscopic measurements with transport coefficients indirectly extrapolated from microscopic measurements, such as NMR relaxometry techniques[20,63−65] or molecular dynamics simulations.[33,66−68]

In summary, we have introduced novel dual-modified compounds in the Li-argyrodite family with the advantage of a rapid preparation technique and monitored their behavior as solid electrolytes by substituting an aliovalent cation for Li$^+$ and increasing the Cl$^-$ content. This firmly proves the efficacy of aliovalent cation doping in this class of superionic argyrodites as a means of increasing the vacancy population and thereby boosting their conductivity. Furthermore, the underlying principles governing the fast ion conduction and diffusion in this class of materials were established. ASSBs employing thiophosphates often operate with cold-pressed

pellets, and hence, it is important that a solid electrolyte exhibits high conductivity in the absence of sintering. The novel super Cl-rich composition $Li_{5.35}Ca_{0.1}PS_{4.5}Cl_{1.55}$ possesses a high room temperature ionic conductivity of 10.2 mS·cm^{-1} in the cold-pressed state with a low activation energy of 0.30 ± 0.01 eV and a very high diffusivity of 1.21×10^{-11} m^2/s. Inter alia, we have introduced PFG-NMR as a powerful method of probing the influence of mechanical modification upon ion transport of solid-electrolyte particles.

■ ASSOCIATED CONTENT

Ⓢ Supporting Information

The Supporting Information is available free of charge at https://pubs.acs.org/doi/10.1021/acs.chemmater.0c03090.

> XRD, Raman, EDX, secondary peak deconvolutions of ^7Li MAS, selected ^7Li 2D NOESY; ^{31}P MAS NMR (super Cl-rich composition); relative density; temperature dependence of the ionic conductivity; Nyquist plot and fitted EIS parameters of y = 0.15 at 195 K; resistance values; selected Rietveld refinements; and comparison of PFG-NMR Arrhenius plots (PDF)

■ AUTHOR INFORMATION

Corresponding Authors

Gillian R. Goward − *Department of Chemistry & Chemical Biology, McMaster University, Hamilton, Ontario L8S 4L8, Canada;* ⓞ orcid.org/0000-0002-7489-3329; Email: goward@mcmaster.ca

Linda F. Nazar − *Department of Chemistry, Department of Chemical Engineering and the Waterloo Institute for Nanotechnology, University of Waterloo, Waterloo, Ontario N2L 3G1, Canada;* ⓞ orcid.org/0000-0002-3314-8197; Email: lfnazar@uwaterloo.ca

Authors

Parvin Adeli − *Department of Chemistry, Department of Chemical Engineering and the Waterloo Institute for Nanotechnology, University of Waterloo, Waterloo, Ontario N2L 3G1, Canada;* ⓞ orcid.org/0000-0002-0311-0382

J. David Bazak − *Department of Chemistry & Chemical Biology, McMaster University, Hamilton, Ontario L8S 4L8, Canada*

Ashfia Huq − *Neutron Scattering Division, Oak Ridge National Laboratory, Oak Ridge, Tennessee 37830, United States*

Complete contact information is available at:
https://pubs.acs.org/10.1021/acs.chemmater.0c03090

Author Contributions

P.A. and J.D.B. contributed equally to this work. P.A. and L.F.N. developed the concept for this study. We thank Dr. Z. Zhang (UWaterloo) for the original suggestion of the divalent dopant. P.A. synthesized the materials and carried out the XRD measurements, electrochemical experiments, and data processing, as well as SEM/EDS and Raman measurements. J.D.B. carried out the ^7Li and ^{31}P NMR investigations and data processing. A.H. recorded the neutron diffraction data, and P.A. performed the Rietveld refinements. P.A., J.D.B., and L.F.N. wrote the manuscript. All the authors contributed to the scientific discussion.

Notes

The authors declare no competing financial interest.

■ ACKNOWLEDGMENTS

■ REFERENCES

(1) Shiau, C.-S. N.; Kaushal, N.; Hendrickson, C. T.; Peterson, S. B.; Whitacre, J. F.; Michalek, J. J. Optimal Plug-In Hybrid Electric Vehicle Design and Allocation for Minimum Life Cycle Cost, Petroleum Consumption, and Greenhouse Gas Emissions. *J. Mech. Des.* **2010**, *132*, 091013.

(2) Hoffert, M. I.; Caldeira, K.; Benford, G.; Criswell, D. R.; Green, C.; Herzog, H.; Jain, A. K.; Kheshgi, H. S.; Lackner, K. S.; Lewis, J. S.; Lightfoot, H. D.; Manheimer, W.; Mankins, J. C.; Mauel, M. E.; Perkins, L. J.; Schlesinger, M. E.; Volk, T.; Wigley, T. M. L. Engineering: Advanced Technology Paths to Global Climate Stability: Energy for a Greenhouse Planet. *Science* **2002**, *298*, 981−987.

(3) Janek, J.; Zeier, W. G. A Solid Future for Battery Development. *Nat. Energy* **2016**, *1*, 16141.

(4) Wang, Q.; Wu, J. F.; Lu, Z.; Ciucci, F.; Pang, W. K.; Guo, X. A New Lithium-Ion Conductor LiTaSiO5: Theoretical Prediction, Materials Synthesis, and Ionic Conductivity. *Adv. Funct. Mater.* **2019**, *29*, 1970253.

(5) Tatsumisago, M.; Nagao, M.; Hayashi, A. Recent Development of Sulfide Solid Electrolytes and Interfacial Modification for All-Solid-State Rechargeable Lithium Batteries. *J. Asian Ceram. Soc.* **2013**, *1*, 17−25.

(6) Li, Y.; Xu, H.; Chien, P.-H.; Wu, N.; Xin, S.; Xue, L.; Park, K.; Hu, Y.-Y.; Goodenough, J. B. A Perovskite Electrolyte That Is Stable in Moist Air for Lithium-Ion Batteries. *Angew. Chem., Int. Ed.* **2018**, *57*, 8587−8591.

(7) Dawson, J. A.; Attari, T. S.; Chen, H.; Emge, S. P.; Johnston, K. E.; Islam, M. S. Elucidating Lithium-Ion and Proton Dynamics in Anti-Perovskite Solid Electrolytes. *Energy Environ. Sci.* **2018**, *11*, 2993−3002.

(8) Li, Y.; Xu, B.; Xu, H.; Duan, H.; Lü, X.; Xin, S.; Zhou, W.; Xue, L.; Fu, G.; Manthiram, A.; Goodenough, J. B. Hybrid Polymer/Garnet Electrolyte with a Small Interfacial Resistance for Lithium-Ion Batteries. *Angew. Chem., Int. Ed.* **2017**, *56*, 753−756.

(9) Cao, C.; Li, Z. B.; Wang, X. L.; Zhao, X. B.; Han, W. Q. Recent Advances in Inorganic Solid Electrolytes for Lithium Batteries. *Front. Energy Res.* **2014**, *2*, 25.

(10) Robertson, A. D.; West, A. R.; Ritchie, A. G. Review of Crystalline Lithium-Ion Conductors Suitable for High Temperature Battery Applications. *Solid State Ionics* **1997**, *104*, 1−11.

(11) Goodenough, J. B.; Singh, P. Solid Electrolytes in Rechargeable Electrochemical Cells. *J. Electrochem. Soc.* **2015**, *162*, A2387−A2392.

(12) Chu, I.-H.; Nguyen, H.; Hy, S.; Lin, Y.-C.; Wang, Z.; Xu, Z.; Deng, Z.; Meng, Y. S.; Ong, S. P. Insights into the Performance Limits of the $Li_7P_3S_{11}$ Superionic Conductor: A Combined First-Principles and Experimental Study. *ACS Appl. Mater. Interfaces* **2016**, *8*, 7843−7853.

(13) Kanno, R.; Murayama, M. Lithium Ionic Conductor Thio-LISICON: The Li2S-GeS2-P2S5 System. *J. Electrochem. Soc.* **2001**, *148*, A742−A746.

(14) Kamaya, N.; Homma, K.; Yamakawa, Y.; Hirayama, M.; Kanno, R.; Yonemura, M.; Kamiyama, T.; Kato, Y.; Hama, S.; Kawamoto, K.; Mitsui, A. A Lithium Superionic Conductor. *Nat. Mater.* **2011**, *10*, 682−686.

(15) Teragawa, S.; Aso, K.; Tadanaga, K.; Hayashi, A.; Tatsumisago, M. Preparation of Li2S-P2S5 Solid Electrolyte from N-Methylforma-

mide Solution and Application for All-Solid-State Lithium Battery. *J. Power Sources* **2014**, *248*, 939−942.

(16) Kato, Y.; Hori, S.; Saito, T.; Suzuki, K.; Hirayama, M.; Mitsui, A.; Yonemura, M.; Iba, H.; Kanno, R. High-Power All-Solid-State Batteries Using Sulfide Superionic Conductors. *Nat. Energy* **2016**, *1*, 16030.

(17) Deiseroth, H.-J.; Kong, S.-T.; Eckert, H.; Vannahme, J.; Reiner, C.; Zaiß, T.; Schlosser, M. Li_6PS_5X: A Class of Crystalline Li-Rich Solids with an Unusually High Li^+ Mobility. *Angew. Chem., Int. Ed.* **2008**, *47*, 755−758.

(18) Li, D.; Cao, L.; Liu, C.; Cao, G.; Hu, J.; Chen, J.; Shao, G. A Designer Fast Li-Ion Conductor $Li_{6.25}PS_{5.25}Cl_{0.75}$ and its Contribution to the Polyethylene Oxide Based Electrolyte. *Appl. Surf. Sci.* **2019**, *493*, 1326−1333.

(19) Wang, S.; Zhang, Y.; Zhang, X.; Liu, T.; Lin, Y.-H.; Shen, Y.; Li, L.; Nan, C.-W. High-Conductivity Argyrodite Li_6PS_5Cl Solid Electrolytes Prepared via Optimized Sintering Processes for All-Solid-State Lithium-Sulfur Batteries. *ACS Appl. Mater. Interfaces* **2018**, *10*, 42279−42285.

(20) Yu, C.; Ganapathy, S.; De Klerk, N. J. J.; Roslon, I.; Van Eck, E. R. H.; Kentgens, A. P. M.; Wagemaker, M. Unravelling Li-Ion Transport from Picoseconds to Seconds: Bulk versus Interfaces in an Argyrodite Li_6PS_5Cl-Li_2S All-Solid-State Li-Ion Battery. *J. Am. Chem. Soc.* **2016**, *138*, 11192−11201.

(21) Rao, R. P.; Sharma, N.; Peterson, V. K.; Adams, S. Formation and Conductivity Studies of Lithium Argyrodite Solid Electrolytes Using In-Situ Neutron Diffraction. *Solid State Ionics* **2013**, *230*, 72−76.

(22) Chen, M.; Yin, X.; Reddy, M. V.; Adams, S. All-Solid-State $MoS_2/Li_6PS_5Br/In$-Li Batteries as a Novel Type of Li/S Battery. *J. Mater. Chem. A* **2015**, *3*, 10698−10702.

(23) Kim, D. H.; Oh, D. Y.; Park, K. H.; Choi, Y. E.; Nam, Y. J.; Lee, H. A.; Lee, S.-M.; Jung, Y. S. Infiltration of Solution-Processable Solid Electrolytes into Conventional Li-Ion-Battery Electrodes for All-Solid-State Li-Ion Batteries. *Nano Lett.* **2017**, *17*, 3013−3020.

(24) Auvergniot, J.; Cassel, A.; Ledeuil, J.-B.; Viallet, V.; Seznec, V.; Dedryvère, R. Interface Stability of Argyrodite Li_6PS_5Cl toward $LiCoO_2$, $LiNi_{1/3}Co_{1/3}Mn_{1/3}O_2$, and $LiMn_2O_4$ in Bulk All-Solid-State Batteries. *Chem. Mater.* **2017**, *29*, 3883−3890.

(25) Evain, M.; Gaudin, E.; Boucher, F.; Petricek, V.; Taulelle, F. Structures and Phase Transitions of the $A7PSe6$ (A = Ag, Cu) Argyrodite-Type Ionic Conductors. I. Ag7PSe6. *Acta Crystallogr., Sect. B: Struct. Sci.* **1998**, *54*, 376−383.

(26) Kraft, M. A.; Culver, S. P.; Calderon, M.; Böcher, F.; Krauskopf, T.; Senyshyn, A.; Dietrich, C.; Zevalkink, A.; Janek, J.; Zeier, W. G. Influence of Lattice Polarizability on the Ionic Conductivity in the Lithium Superionic Argyrodites Li_6PS_5X (X = Cl, Br, I). *J. Am. Chem. Soc.* **2017**, *139*, 10909−10918.

(27) Adeli, P.; Bazak, J. D.; Park, K. H.; Kochetkov, I.; Huq, A.; Goward, G. R.; Nazar, L. F. Boosting Solid-State Diffusivity and Conductivity in Lithium Superionic Argyrodites by Halide Substitution. *Angew. Chem., Int. Ed.* **2019**, *58*, 8681−8686.

(28) Jung, W. D.; Kim, J.-S.; Choi, S.; Kim, S.; Jeon, M.; Jung, H.-G.; Chung, K. Y.; Lee, J.-H.; Kim, B.-K.; Lee, J.-H.; Kim, H. Superionic Halogen-Rich Li-Argyrodites Using In Situ Nanocrystal Nucleation and Rapid Crystal Growth. *Nano Lett.* **2020**, *20*, 2303−2309.

(29) Yu, C.; Li, Y.; Willans, M.; Zhao, Y.; Adair, K. R.; Zhao, F.; Li, W.; Deng, S.; Liang, J.; Banis, M. N.; Li, R.; Huang, H.; Zhang, L.; Yang, R.; Lu, S.; Huang, Y.; Sun, X. Superionic Conductivity in Lithium Argyrodite Solid-State Electrolyte by Controlled Cl-Doping. *Nano Energy* **2020**, *69*, 104396−104406.

(30) Arnold, W.; Buchberger, D. A.; Li, Y.; Sunkara, M.; Druffel, T.; Wang, H. Halide Doping Effect on Solvent-Synthesized Lithium Argyrodites Li_6PS_5X (X= Cl, Br, I) Superionic Conductors. *J. Power Sources* **2020**, *464*, 228158−228165.

(31) Zhou, L.; Park, K.-H.; Sun, X.; Lalère, F.; Adermann, T.; Hartmann, P.; Nazar, L. F. Solvent-Engineered Design of Argyrodite Li_6PS_5X (X = Cl, Br, I) Solid Electrolytes with High Ionic Conductivity. *ACS Energy Lett.* **2019**, *4*, 265−270.

(32) Bernges, T.; Culver, S. P.; Minafra, N.; Koerver, R.; Zeier, W. G. Competing Structural Influences in the Li Superionic Conducting Argyrodites $Li_6PS_{5-x}Se_xBr$ ($0 \leq x \leq 1$) upon Se Substitution. *Inorg. Chem.* **2018**, *57*, 13920−13928.

(33) De Klerk, N. J. J.; Rosłoń, I.; Wagemaker, M. Diffusion Mechanism of Li Argyrodite Solid Electrolytes for Li-Ion Batteries and Prediction of Optimized Halogen Doping: The Effect of Li Vacancies, Halogens, and Halogen Disorder. *Chem. Mater.* **2016**, *28*, 7955−7963.

(34) Feng, X.; Chien, P.-H.; Wang, Y.; Patel, S.; Wang, P.; Liu, H.; Immediato-Scuotto, M.; Hu, Y.-Y. Enhanced Ion Conduction by Enforcing Structural Disorder in Li-Deficient Argyrodites $Li_{6-x}PS_{5-x}Cl_{1+x}$. *Energy Storage Mater.* **2020**, *30*, 67−73.

(35) Minafra, N.; Culver, S. P.; Krauskopf, T.; Senyshyn, A.; Zeier, W. G. Effect of Si Substitution on the Structural and Transport Properties of Superionic Li-Argyrodites. *J. Mater. Chem. A* **2018**, *6*, 645−651.

(36) Song, Y. B.; Kim, D. H.; Kwak, H.; Han, D.; Kang, S.; Lee, J. H.; Bak, S.-M.; Nam, K.-W.; Lee, H.-W.; Jung, Y. S. Tailoring Solution-Processable Li Argyrodites $Li_{6+x}P_{1-x}MxS_5I$ (M= Ge, Sn) and Their Microstructural Evolution Revealed by Cryo-TEM for All-Solid-State Batteries. *Nano Lett.* **2020**, *20*, 4337−4345.

(37) Ohno, S.; Helm, B.; Fuchs, T.; Dewald, G.; Kraft, M. A.; Culver, S. P.; Senyshyn, A.; Zeier, W. G. Further Evidence for Energy Landscape Flattening in the Superionic Argyrodites $Li_{6+x}P_{1-x}MxS_5I$ (M= Si, Ge, Sn). *Chem. Mater.* **2019**, *31*, 4936−4944.

(38) Schneider, H.; Du, H.; Kelley, T.; Leitner, K.; ter Maat, J.; Scordilis-Kelley, C.; Sanchez-Carrera, R.; Kovalev, I.; Mudalige, A.; Kulisch, J.; Safont-Sempere, M. M.; Hartmann, P.; Weiβ, T.; Schneider, L.; Hinrichsen, B. A Novel Class of Halogen-Free, Super-Conductive Lithium Argyrodites: Synthesis and Characterization. *J. Power Sources* **2017**, *366*, 151−160.

(39) Zhang, Z.; Sun, Y.; Duan, X.; Peng, L.; Jia, H.; Zhang, Y.; Shan, B.; Xie, J. Design and Synthesis of Room Temperature Stable Li-Argyrodite Superionic Conductors via Cation Doping. *J. Mater. Chem. A* **2019**, *7*, 2717−2722.

(40) Schneider, H.; Sedlmaier, S. J.; Du, H.; Kelley, T.; Leitner, K.; ter Maat, J.; Scordilis-Kelley, C.; Mudalige, A.; Kulisch, J.; Schneider, L. Stabilization of Highly Conductive Lithium Argyrodites by Means of Lithium Substitution: The Case of $Li_6Fe_{0.5}PS_6$. *ChemistrySelect* **2019**, *4*, 3351−3354.

(41) Zhang, Z.; Zhang, J.; Jia, H.; Peng, L.; An, T.; Xie, J. Enhancing Ionic Conductivity of Solid Electrolyte by Lithium Substitution in Halogenated Li-Argyrodite. *J. Power Sources* **2020**, *450*, 227601−227607.

(42) Hikima, K.; Phuc, N. H. H.; Tsukasaki, H.; Mori, S.; Muto, H.; Matsuda, A. High Ionic Conductivity of Multivalent Cation Doped Li_6PS_5Cl Solid Electrolytes Synthesized by Mechanical Milling. *RSC Adv.* **2020**, *10*, 22304−22310.

(43) Tsujimura, T.; Suzuki, N.; Aihara, Y. Solid Electrolyte and Lithium Battery Including the Same. U.S Patent 20,170,187,066 A1, June 29, 2017.

(44) Kuhn, A.; Duppel, V.; Lotsch, B. V. Tetragonal $Li_{10}GeP_2S_{12}$ and Li_7GePS_8 − Exploring the Li Ion Dynamics in LGPS Li Electrolytes. *Energy Environ. Sci.* **2013**, *6*, 3548−3552.

(45) Kaus, M.; Stöffler, H.; Yavuz, M.; Zinkevich, T.; Knapp, M.; Ehrenberg, H.; Indris, S. Local Structures and Li Ion Dynamics in a $Li_{10}SnP_2S_{12}$-Based Composite Observed by Multinuclear Solid-State NMR Spectroscopy. *J. Phys. Chem. C* **2017**, *121*, 23370−23376.

(46) Griffith, K. J.; Wiaderek, K. M.; Cibin, G.; Marbella, L. E.; Grey, C. P. Niobium Tungsten Oxides for High-Rate Lithium-Ion Energy Storage. *Nature* **2018**, *559*, 556−563.

(47) Dorai, A.; Kuwata, N.; Takekawa, R.; Kawamura, J.; Kataoka, K.; Akimoto, J. Diffusion Coefficient of Lithium Ions in Garnet-Type $Li_{6.5}La_3Zr_{1.5}Ta_{0.5}O_{12}$ Single Crystal Probed by ^7Li Pulsed Field Gradient-NMR Spectroscopy. *Solid State Ionics* **2018**, *327*, 18−26.

(48) Yu, C.; van Eijck, L.; Ganapathy, S.; Wagemaker, M. Synthesis, Structure and Electrochemical Performance of the Argyrodite

Li$_6$PS$_5$Cl Solid Electrolyte for Li-Ion Solid State Batteries. *Electrochim. Acta* **2016**, *215*, 93−99.

(49) Boulineau, S.; Courty, M.; Tarascon, J.-M.; Viallet, V. Mechanochemical Synthesis of Li-Argyrodite Li$_6$PS$_5$X (X = Cl, Br, I) as Sulfur-Based Solid Electrolytes for All Solid State Batteries Application. *Solid State Ionics* **2012**, *221*, 1−5.

(50) Boulineau, S.; Tarascon, J.-M.; Leriche, J.-B.; Viallet, V. Electrochemical Properties of All-Solid-State Lithium Secondary Batteries Using Li-Argyrodite Li$_6$PS$_5$Cl as Solid Electrolyte. *Solid State Ionics* **2013**, *242*, 45−48.

(51) Yu, C.; Ganapathy, S.; Hageman, J.; Van Eijck, L.; Van Eck, E. R. H.; Zhang, L.; Schwietert, T.; Basak, S.; Kelder, E. M.; Wagemaker, M. Facile Synthesis toward the Optimal Structure-Conductivity Characteristics of the Argyrodite Li$_6$PS$_5$Cl Solid-State Electrolyte. *ACS Appl. Mater. Interfaces* **2018**, *10*, 33296−33306.

(52) Kraft, M. A.; Ohno, S.; Zinkevich, T.; Koerver, R.; Culver, S. P.; Fuchs, T.; Senyshyn, A.; Indris, S.; Morgan, B. J.; Zeier, W. G. Inducing High Ionic Conductivity in the Lithium Superionic Argyrodites Li$_{6+x}$P$_{1-X}$Ge$_x$S$_5$I for All-Solid-State Batteries. *J. Am. Chem. Soc.* **2018**, *140*, 16330−16339.

(53) Moon, C. K.; Lee, H.-J.; Park, K. H.; Kwak, H.; Heo, J. W.; Choi, K.; Yang, H.; Kim, M.-S.; Hong, S.-T.; Lee, J. H.; Jung, Y. S. Vacancy-Driven Na$^+$ Superionic Conduction in New Ca-Doped Na$_3$PS$_4$ for All-Solid-State Na-Ion Batteries. *ACS Energy Lett.* **2018**, *3*, 2504−2512.

(54) Zhou, L.; Assoud, A.; Zhang, Q.; Wu, X.; Nazar, L. F. New Family of Argyrodite Thioantimonate Lithium Superionic Conductors. *J. Am. Chem. Soc.* **2019**, *141*, 19002−19013.

(55) Minafra, N.; Kraft, M. A.; Bernges, T.; Li, C.; Schlem, R.; Morgan, B. J.; Zeier, W. G. Local Charge Inhomogeneity and Lithium Distribution in the Superionic Argyrodites Li$_6$PS$_5$X (X= Cl, Br, I). *Inorg. Chem.* **2020**, *59*, 11009−11019.

(56) Israel Science and Technology Directory. List of Periodic Table Elements Sorted by: Abundance in Earth's Crust. https://www.science.co.il/elements/?s=Earth (accessed 15-07-2019).

(57) Bain, A. D. Chemical Exchange in NMR. *Prog. Nucl. Magn. Reson. Spectrosc.* **2003**, *43*, 63−103.

(58) Shin, B. R.; Nam, Y. J.; Oh, D. Y.; Kim, D. H.; Kim, J. W.; Jung, Y. S. Comparative Study of TiS$_2$/Li-In All-Solid-State Lithium Batteries Using Glass-Ceramic Li$_3$PS$_4$ and Li$_{10}$GeP$_2$S$_{12}$ Solid Electrolytes. *Electrochim. Acta* **2014**, *146*, 395−402.

(59) Bron, P.; Johansson, S.; Zick, K.; Der Günne, J. S. A.; Dehnen, S.; Roling, B. Li$_{10}$SnP$_2$S$_{12}$: An Affordable Lithium Superionic Conductor. *J. Am. Chem. Soc.* **2013**, *135*, 15694−15697.

(60) Callaghan, T. *Principles of Nuclear Magnetic Resonance Microscopy*; Clarendon Press: Oxford, 1991; pp 57−63.

(61) Kärger, J. Diffusion Measurements by NMR Techniques. In *Adsorption and Diffusion*; Karge, H. G., Weitkamp, J., Eds.; Molecular Sieves; Springer: Berlin, Heidelberg, 2008; Vol. 7, pp 85−133.

(62) Heitjans, P.; Indris, S. Diffusion and Ionic Conduction in Nanocrystalline Ceramics. *J. Phys.: Condens. Matter* **2003**, *15*, R1257−R1289.

(63) Epp, V.; Gün, Ö.; Deiseroth, H.-J.; Wilkening, M. Long-Range Li$^+$ Dynamics in the Lithium Argyrodite Li$_7$PSe$_6$ as Probed by Rotating-Frame Spin-Lattice Relaxation NMR. *Phys. Chem. Chem. Phys.* **2013**, *15*, 7123−7132.

(64) Stöffler, H.; Zinkevich, T.; Yavuz, M.; Senyshyn, A.; Kulisch, J.; Hartmann, P.; Adermann, T.; Randau, S.; Richter, F. H.; Janek, J.; Indris, S.; Ehrenberg, H. Li$^+$-Ion Dynamics in β-Li$_3$PS$_4$ Observed by NMR: Local Hopping and Long-Range Transport. *J. Phys. Chem. C* **2018**, *122*, 15954−15965.

(65) Hanghofer, I.; Brinek, M.; Eisbacher, S. L.; Bitschnau, B.; Volck, M.; Hennige, V.; Hanzu, I.; Rettenwander, D.; Wilkening, H. M. R. Substitutional Disorder: Structure and Ion Dynamics of the Argyrodites Li$_6$PS$_5$Cl, Li$_6$PS$_5$Br and Li$_6$PS$_5$I. *Phys. Chem. Chem. Phys.* **2019**, *21*, 8489−8507.

(66) Ong, S. P.; Mo, Y.; Richards, W. D.; Miara, L.; Lee, H. S.; Ceder, G. Phase Stability, Electrochemical Stability and Ionic Conductivity of the Li$_{10\pm1}$MP$_2$X$_{12}$ (M = Ge, Si, Sn, Al or P, and X = O, S or Se) Family of Superionic Conductors. *Energy Environ. Sci.* **2013**, *6*, 148−156.

(67) He, X.; Zhu, Y.; Mo, Y. Origin of Fast Ion Diffusion in Super-Ionic Conductors. *Nat. Commun.* **2017**, *8*, 15893.

(68) De Klerk, N. J. J.; Van Der Maas, E.; Wagemaker, M. Analysis of Diffusion in Solid-State Electrolytes through MD Simulations, Improvement of the Li-Ion Conductivity in β-Li$_3$PS$_4$ as an Example. *ACS Appl. Energy Mater.* **2018**, *1*, 3230−3242.